Journal of Solid State Chemistry 183 (2010) 2917–2924

Contents lists available at ScienceDirect

Journal of Solid State Chemistry

journal homepage: www.elsevier.com/locate/jssc

Structure, bonding, and magnetic response in two complex borides: $Zr_2Fe_{1-\delta}Ru_{5+\delta}B_2$ and $Zr_2Fe_{1-\delta}(Ru_{1-x}Rh_x)_{5+\delta}B_2$

Jakoah Brgoch [a], Steven Yeninas [b,c], Ruslan Prozorov [b,c], Gordon J. Miller [a,c,*]

[a] Department of Chemistry, Iowa State University, Ames, IA 50011, USA
[b] Department of Physics and Astronomy, Iowa State University, Ames, IA 50011, USA
[c] Ames Laboratory, Iowa State University, Ames, IA 50011, USA

ARTICLE INFO

Article history:
Received 28 April 2010
Received in revised form
15 September 2010
Accepted 19 September 2010
Available online 1 October 2010

Keywords:
Intermetallic borides
TB-LMTO-ASA
SQUID magnetometry

ABSTRACT

Polycrystalline samples of two complex intermetallic borides $Zr_2Fe_{1-\delta}Ru_{5+\delta}B_2$ and $Zr_2Fe_{1-\delta}(Ru_{1-x}Rh_x)_{5+\delta}B_2$ (δ=ca. 0.10; x=0.20) were synthesized by high-temperature methods and characterized by single-crystal X-ray diffraction, energy dispersive spectroscopy, and magnetization measurements. Both structures are variants of $Sc_2Fe(Ru_{1-x}Rh_x)_5B_2$ and crystallize in the space group *P4/mbm* (no. 127) with the $Ti_3Co_5B_2$-type structure. These structures contain single-atom, Fe-rich Fe/Ru or Fe/Ru/Rh chains along the *c*-axis with an interatomic metal-metal distance of 3.078(1) Å, a feature which makes them viable for possible low-dimensional temperature-dependent magnetic behavior. Magnetization measurements indicated weak ferrimagnetic ordering with ordering temperatures ca. 230 K for both specimens. Tight-binding electronic structure calculations on a model "$Zr_2FeRu_5B_2$" using LDA yielded a narrow peak at the Fermi level assigned to Fe–Fe antibonding interactions along the *c*-axis, a result that indicates an electronic instability toward ferromagnetic coupling along these chains. Spin-polarized calculations of various magnetic models were examined to identify possible magnetic ordering within and between the single-atom, Fe-rich chains.

1. Introduction

Many structural variants of the tetragonal $Ti_3Co_5B_2$-type [1] have recently been discovered [2–4]. The original structure type consists of stacked cobalt nets that form trigonal, tetragonal, and pentagonal prisms in which boron atoms occupy the trigonal prisms and titanium atoms occupy the tetragonal and pentagonal prisms. One variant, $Sc_2FeRu_5B_2$, [3–5] contains ruthenium nets with boron, again, in the trigonal prisms, scandium in the pentagonal prisms, and iron replacing titanium in the square prisms. The resulting crystal structure creates chains of iron atoms with interatomic distances of approximately 3.0 Å, and provides an opportunity to study possible low-dimensional itinerant magnetism. In fact, other structures of this type exhibit a wide range of magnetic ordering including ferromagnetism, ferrimagnetism, and antiferromagnetism, depending on the valence electron count. For instance, substituting rhodium for ruthenium has successfully yielded the isostructural series $Sc_2Fe(Ru_{1-x}Rh_x)_5B_2$ (x=0–1) with the compounds with low Rh content (x=0–0.4) exhibiting antiferromagnetism, while those with higher Rh content (x=0.6–1) are ferromagnetic [4,5].

Samolyuk et al. [6] theoretically investigated the change in magnetic order as a function of valence electron count for this pseudo-quaternary system, $Sc_2Fe(Ru_{1-x}Rh_x)_5B_2$ (x=0–1), by calculating effective exchange parameters based on the linear-response method in the long wavelength approximation. The exchange parameters between Fe atoms and the surrounding Ru/Rh mixed sites indicated strong coupling (J_{Fe-Rh}=3.77 MeV) for the fully substituted Rh case (x=1), and very weak coupling (J_{Fe-Ru}=0.07 MeV) for the Ru case (x=0). Therefore, the magnetic ordering of the system is significantly influenced by the valence electron count, which affects features of certain nearest neighbor orbital interactions near the corresponding Fermi levels. Other strategies to probe the magnetic ordering as a function of valence electron count in these complex phases includes replacing Sc with Group 4 metals and Fe atoms with surrounding 3*d* metals.

Herein, we report on two new compounds adopting the tetragonal $Ti_3Co_5B_2$-type with compositions $Zr_2Fe_{1-\delta}Ru_{5+\delta}B_2$ and $Zr_2Fe_{1-\delta}(Ru_{1-x}Rh_x)_{5+\delta}B_2$, in which Sc was replaced with Zr in $Sc_2Fe(Ru_{1-x}Rh_x)_5B_2$. The quaternary phase was originally observed as the major product in an attempt to replace Ti with Zr in $Ti_9Fe_2Ru_{18}B_8$, i.e., "$Zr_9Fe_2Ru_{18}B_8$". The electronic structures, including a chemical bonding analysis obtained by Crystal Orbital Hamiltonian Population (COHP) curves are presented to interpret structural features and their magnetic behavior.

* Corresponding author.
E-mail address: gmiller@iastate.edu (G.J. Miller).

0022-4596/$ - see front matter © 2010 Elsevier Inc. All rights reserved.
doi:10.1016/j.jssc.2010.09.025

2. Experimental section

2.1. Synthesis

Polycrystalline samples loaded as "$Zr_2FeRu_5B_2$" and "$Zr_2FeRu_4RhB_2$" were synthesized by arc-melting stoichiometric mixtures of the elements in a water-cooled copper crucible under a purified argon atmosphere using thoriated tungsten as a second electrode. The starting materials (Zr: pieces, 99.99%, Material Preparation Center, Ames National Lab; Fe: chips, 99.98%, Sigma Aldrich; Ru: pieces, 99.99%, Material Preparation Center, Ames National Lab; Rh: pieces, 99.95%, Material Preparation Center, Ames National Lab; B: crystalline pieces, 99.999%, Alfa Aesar) were weighed in the corresponding stoichiometric ratios with a total mass of approximately 0.6 g and arc-melted a minimum of six times with turning to ensure homogeneity. The argon was purified over titanium sponge at 800 °C.

The as-cast products were gray in appearance, and single crystals could be selected from the arc-melted samples. Annealing was completed in sealed tantalum tubes within silica jackets under reduced pressure (ca. 50×10^{-6} Torr). Samples were heated from room temperature to 1000 °C at 25 °C/h and held approximately 14 days before quenching to ambient temperature. Samples were then analyzed by powder X-ray diffraction, energy dispersive spectroscopy, and single crystal X-ray diffraction. The purity of the samples was checked by the powder X-ray diffraction on a Huber 670 Guinier (image-plate) camera with Cu $K\alpha_1$ radiation ($\lambda=1.540598$ Å). All products were visually stable to decomposition in air at room temperature over several months. Lattice parameters were refined from the powder diffraction pattern using the program *Rietica* [7].

Rhodium substitution was attempted for the entire range ($x=0$–1) in "$Zr_2Fe_1(Ru_{1-x}Rh_x)_5B_2$", but the desired phase is present as the major phase only for $x\leq0.2$. Loaded samples richer in Rh, $x=0.4$–1, yielded $Zr(Ru/Rh)_3$ as the primary phase. Moreover, as discussed below, repeated synthesis of loaded "$Zr_2FeRu_5B_2$" always resulted in Fe deficiency, ranging from $\delta=0.13(8)$ to 0.37(5) in $Zr_2Fe_{1-\delta}Ru_{5+\delta}B_2$. Through a combination of synthetic variation and X-ray powder diffraction, the maximum Fe deficiency is ca. $\delta=0.50$ [8]. After various annealing strategies, however, the highest quality products characterized were those richest in Fe content. Therefore, we restricted our efforts to optimize yields of the Fe-richest samples, $Zr_2Fe_{1-\delta}Ru_{5+\delta}B_2$ and $Zr_2Fe_{1-\delta}(Ru_{1-x}Rh_x)_{5+\delta}B_2$, for further experimental and theoretical studies.

2.2. Structure determination

Single crystals were selected from the annealed samples and fixed on a glass capillary. Data were collected using a STOE IPDS-II diffractometer with graphite monochromated Mo $K\alpha$ ($\lambda=0.71073$ Å) radiation. Reflections were collected in two sets of frames: the first with $\phi=78^\circ$ and ω ranging from 11° to 160° with 1° increments (149 frames), the second with $\phi=258^\circ$ and ω ranging from 0° to 62° with 1° increments (62 frames), for 211 total frames with an exposure time of 5 min per frame. Intensities were corrected by numerical absorption correction using *X-RED* and the crystal shape optimized with the aid of *X-SHAPE* [9–10] software. The structures were refined by full matrix least-squares refinement based of F^2 with the *SHELXTL* package [11], using anisotropic displacement for all metal atom sites and isotropic displacement for the boron site. All crystal structure drawings were produced using the program *Diamond* [12].

2.3. Chemical analysis

Characterization was accomplished using a variable pressure scanning electron microscope (Hitachi S-2460 N) and energy-dispersive spectroscopy (EDS) (Oxford Instruments Isis X-ray analyzer). Samples were first polished with a 1-μm diamond slurry and then coated with approximately 20 nm of carbon. The samples were examined at 20 kV and a beam current ca. 0.5 nA that produced 3000 cps with 30% deadtime. Spectra were collected for 80 s. An Oxford Instruments *Tetra* backscattered electron (BSE) detector was used to image the samples using the BSE signal. Multiple points were examined in each phase within multiple grains of a specimen. Compositional estimates were calculated using Oxford's *SEMQuant* software to correct intensities for matrix effects. Pure element standards were used as intensity references for Ru, Rh, Fe, and Zr; B was not quantitatively analyzed. Atomic size, absorption, and fluorescence were corrected using a standard ZAF matrix correction and used to convert intensity ratios to compositions.

2.4. Electronic structure calculations

Calculations of the electronic and possible magnetic structures were performed using the tight-binding, linear muffin-tin orbital method with the atomic spheres approximation (TB-LMTO-ASA) [13,14] using the Stuttgart code [15]. Exchange and correlation were treated by the local density approximation (LDA) and the local spin density approximation (LSDA) [16]. In the ASA method, space is filled with overlapping Wigner–Seitz (WS) spheres. The symmetry of the potential is considered spherical inside each WS sphere and a combined correction is used to take into account the overlapping part. The WS radii are: 1.50–1.55 Å (Ru), 1.70 Å (Zr), 1.58 Å (Fe), and 0.98 Å (B). No empty spheres were necessary in these models, and the WS sphere overlaps were limited to no larger than 16%. The basis set for the calculations included Ru (5*s*, 5*p*, 4*d*, 4*f* downfolded), Zr (5*s*, 5*p*, 4*d*, 4*f* downfolded), Fe (4*s*, 4*p*, 3*d*), B (2*s*, 2*p*, 3*d* downfolded) wavefunctions. The convergence criteria was set to 1×10^{-4} eV. A mesh of 54 **k** points in the irreducible wedge of the first Brillouin zone was used to obtain all integrated values, including the density of states (DOS) and Crystal Orbital Hamiltonian Population (COHP) curves [17].

2.5. Magnetization measurements

The magnetization measurements were collected on the two samples using a *Quantum Design* MPMS SQUID magnetometer over the temperature range 5–300 K with applied fields of up to 5 T. The samples were placed in gel capsules for measurement. The three largest polycrystalline pieces of sample I were manually selected and secured using *Apiezon* N grease. Sample II was a fine powder, which was securely compacted using Kimwipes®. The diamagnetic core contributions to the magnetization are ca. -1.62×10^{-4} emu/mol for both samples.

3. Results and discussion

All high-temperature synthetic attempts to prepare $Zr_2Fe_{1-\delta}Ru_{5+\delta}B_2$ and $Zr_2Fe_{1-\delta}(Ru_{1-x}Rh_x)_{5+\delta}B_2$ yielded some Fe deficiency, i.e., $\delta>0$, and a maximum Rh content of $x=0.2$. The highest quality products, as determined by a combination of EDS and powder and single crystal X-ray diffraction, were those samples richest in Fe. Thus, in the following discussion, "sample I" refers to the quaternary phase characterized as $Zr_2Fe_{0.87(8)}Ru_{5.13}B_2$, and "sample II" labels the quintinary phase, $Zr_2Fe_{0.82}(Ru_{0.8}Rh_{0.2})_{5.18}B_2$.

3.1. Chemical analysis

EDS was employed to determine qualitatively the composition and elemental distribution of the prepared samples, as well as to compare with subsequent refinements from the single crystal X-ray diffraction. An X-ray map (see supporting information) was employed to identify the distribution of the phases in relation to each other, with compositional information collected for each phase. Two phases were identified present in bulk pieces of sample I: the major phase showed an average molar ratio of metals to be 2.2(1) Zr:0.7(1) Fe:5.11(2) Ru, which is close to the loaded metals composition of 2 Zr:1 Fe:5 Ru. The minor phase was determined to have an average stoichiometric composition of 1.1(1) Fe:2.00(7) Ru. This phase was not observed in powder X-ray diffraction patterns (see Supporting Information for X-ray powder diffraction patterns of both samples), and, as a result, is less than ca. 5% of the total crystalline component in the sample. EDS on sample II was also collected and showed the presence of multiple phases. The major phase yielded an average molar ratio of metals to be 2.3(1) Zr:0.7(1) Fe:3.99(8) Ru:0.99(9) Rh, which is very close to the loaded metals composition. This sample, however, also contains inclusions of elemental Zr, 0.51(3) Fe:0.49(3) Ru ("RuFe"), 1.0(3) Zr:0.50(4) Ru:2.33(9) Rh, and 2.6(3) Zr:1.0(2) Fe:2.5(5) Ru:5.8(1) Rh. Boron was not quantitatively analyzed for any of the samples.

Refinements of site occupancies based on single crystal X-ray diffraction data, discussed in more detail in the next section, always led to mixing of Fe and either Ru or a Ru/Rh mixture on a single crystallographic site (Wyckoff 2*a* site) to eliminate non-positive definite displacement parameters at this position. The Rh and Ru contents were fixed according to the loading composition. Refined compositions averaged over three single crystal measurements for each sample were $Zr_2Fe_{0.87(8)}Ru_{5.13}B_2$ for sample I and $Zr_2Fe_{0.82(3)}(Ru/Rh)_{5.18}B_2$ for sample II. These refined compositions agree with the EDS analysis of the majoring components in each sample.

3.2. Structure determination

The observed powder X-ray diffraction patterns of samples I and sample II yielded, respectively, refined lattice parameters of $a=9.3361(1)$; $c=3.0700(1)$ and $a=9.3489(1)$; $c=3.0663(1)$. The volume increases by less than 1% with the substitution of Rh for Ru. A volume increase of a similar magnitude is also observed in the substitutional variants of the scandium analogues [5]. The results of single crystal diffraction on specimens extracted from annealed samples I and II are listed in Tables 1 and 2. These (pseudo)-quaternary derivative of the tetragonal $Ti_3Co_5B_2$-type structure is shown in Fig. 1 as a projection along the [0 0 1] direction. Its structure contains distorted pentagonal, square, and trigonal prisms formed by Ru/Rh atoms. Zr atoms occupy the 4*g* sites within each pentagonal prism, while B atoms occupy the 4*g* sites in every trigonal prism. The magnetically active element, Fe, is located within the 2*a* distorted square prisms and forms chains along the [0 0 1] direction, as in the $Sc_2Fe(Ru_{1-x}Rh_x)_5B_2$ series. Here, however, single crystal data always indicate a mixture of Fe and Ru or Ru/Rh atoms at the 2*a* sites in both samples.

The smaller size and valence electron count of Ru make it the likely candidate over Zr to co-occupy the centers of square prisms (2*a* sites) with the Fe atoms. An alternative refinement strategy in which Zr and Fe were mixed at the 2*a* sites did not achieve the statistical agreement that the refinements in Tables 1 and 2 yielded. Furthermore, ZrRu adopts the CsCl-type structure with Zr–Ru nearest neighbor distances of 2.817 Å [18] while the distorted cubic prisms in these complex borides have much

Table 1
Crystallographic data for samples I and II at 293(2) K.

Specimen	Sample I	Sample II
Refined formula	$Zr_2Fe_{0.91(3)}Ru_{5.09}B_2$	$Zr_2Fe_{0.84(4)}(Ru/Rh)_{5.16}B_2$
F.W. (g/mol); $F(0\,0\,0)$	769.48; 675	774.51; 680
Space group; Z	$P4/mbm$ (No. 127); 2	$P4/mbm$ (No. 127); 2
Lattice parameters (Å)	$a=9.3361(1)$ $c=3.0700(1)$	$a=9.3489(1)$ $c=3.0663(1)$
Volume (Å^3)	267.60(1)	268.00(1)
d_{calc} (Mg/m^3)	9.434	9.449
Absorption correction	Numerical	Numerical
μ (mm^{-1})	19.781	20.023
θ range (deg.)	$3.08<\theta<33.29$	$3.08<\theta<33.29$
hkl ranges	$-14<h<14$, $-14<k<12$, $-4<l<4$	$-14<h<14$, $-14<k<12$, $-4<l<4$
No. reflections; R_{int}	3776; 0.0427	4187; 0.0399
No. independent reflections	318	327
No. parameters	19	21
R_1; wR_2 (all I)	0.0436; 0.0761	0.0397; 0.1036
Goodness of fit	1.447	1.072
Diffraction peak and hole (e$^-$/Å^3)	2.227 and −3.692	1.660 and −3.298

Table 2
Atomic coordinates and equivalent isotropic displacement parameters of (a) sample I and (b) sample II. U_{eq} is defined as one-third of the trace of the orthogonalized U^{ij} tensor (Å^2 $\times 10^2$).

Atom	Wyckoff Position	Occ.	x	y	z	U_{eq}
(a)						
Ru1	8*j*	1	0.2158(1)	0.0706(1)	$\frac{1}{2}$	6(1)
Ru2	2*c*	1	$\frac{1}{2}$	0	$\frac{1}{2}$	5(1)
Zr	4*g*	1	0.3244(1)	0.8244(1)	0	6 (1)
Fe/Ru	2*a*	0.91(3)/0.09	0	0	0	4(1)
B	4*g*	1	0.3741(2)	0.1259(2)	0	13(3)
(b)						
Ru/Rh1	8*j*	1	0.2167(1)	0.07059(8)	$\frac{1}{2}$	7(1)
Ru/Rh2	2*c*	1	$\frac{1}{2}$	0	$\frac{1}{2}$	6(1)
Zr	4*g*	1	0.3243 (1)	0.8243(1)	0	7(1)
Fe/(Ru/Rh)	2*a*	0.84(4)/0.16	0	0	0	6(1)
B	4*g*	1	0.377(1)	0.127(1)	0	10(2)

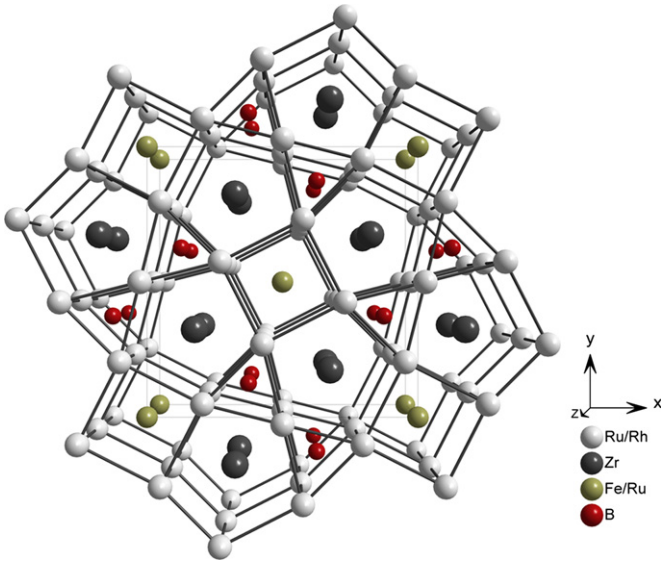

Fig. 1. Perspective view of the crystal structure of $Zr_2Fe_{0.87}Ru_{5.13}B_2$ (sample I) along the [0 0 1] direction. $Zr_2Fe_{0.82}(Ru/Rh)_{5.18}B_2$ (sample II) is isostructural with possible random distribution of Ru and Rh atoms.

shorter distances of 2.623 and 2.630 Å, respectively, for $Zr_2Fe_{0.87(8)}Ru_{5.13}B_2$ and $Zr_2Fe_{0.82(3)}(Ru/Rh)_{5.18}B_2$.

The magnetically active Fe atoms are separated by at least 3.1 Å along the [0 0 1] direction and 6.7 Å along the {1 1 0} directions in sample I, whereas $Sc_2FeRu_{5-x}Rh_xB_2$ shows distances of at least 3.01 Å along the [0 0 1] direction and 6.6 Å along the {1 1 0} directions, dependent on the Rh concentration. The Ru–Ru distances are nearly identical in both the Zr and Sc phases with distances between 2.74 and 3.00 Å. Zr–Ru contacts have an average length of 2.89 Å compared to the Sc–Ru average length of 2.84 Å. Such similar distances among the majority components may result in comparable behavior of the magnetically active atoms; however, the metal atom mixing at the 2*a* sites may also dramatically alter the long-range magnetic order.

3.3. Electronic structure and chemical bonding

The electronic structure of the hypothetical structure "$Zr_2FeRu_5B_2$", with a valence electron (VE) count of 62 electrons, was investigated computationally to interpret the electronic structure. This model was selected after first examining the effect of Fe/Ru mixing at the 2*a* site on the theoretical electronic structure. The total DOS curves of three models, "$Zr_2FeRu_5B_2$", "$Zr_2Fe_{0.5}Ru_{5.5}B_2$", and "$Zr_2Ru_6B_2$" were compared to determine the effect any atomic mixing on the electronic structure. The resulting curves, illustrated in the supporting information, show very slight differences. As a result, "$Zr_2FeRu_5B_2$", with the 2*a* site fully occupied by Fe atoms, was utilized to investigate the electronic structures and bonding in $Zr_2Fe_{1-\delta}(Ru_{1-x}Rh_x)_{5+\delta}B_2$.

Analysis of both the non-spin polarized (LDA) and spin polarized (LSDA) total DOS curves shows nonzero values at the Fermi level (E_F), suggesting metallic behavior. Moreover, the E_F falls on a local maximum of the DOS curve from the LDA calculation, a result that is indicative of a possible electronic instability. When spin polarization is taken into account, a narrow pseudogap develops from 60 to 63 VEs (−0.25 to 0.25 eV). The LSDA DOS curves are shown in Fig. 2 with E_F (62 VE) set as the energy reference. The DOS curves show contributions from the valence orbitals of all elements throughout the entire energy range, but with some indications of the relative electronegativities of these elements.

The bands 7.5–10 eV below the Fermi level are mostly B 2*s*-orbitals with some mixing of Ru and Zr 5*s*-orbitals as well. Between −6 eV and E_F, the states are largely Ru 4*d*-orbitals with some Ru 5*s*-orbitals present between −6 and −4 eV. In the same region, there are significant contributions from B 2*p*-orbitals. Zr valence orbitals constitute ca. 25% of the total DOS between −6 eV and E_F and increase to ca. 50% of the total DOS above the pseudogap. The spin polarized partial DOS of Fe atom orbitals falls between −5 and +3 eV, with the majority spin states having 68% of the occupied states and the minority spin states having 32%. In addition, the minority bands are compressed into a 2 eV window above E_F. As a result, the mostly filled Ru orbitals below the Fermi level and the virtual Zr orbitals above E_F, combined with the strong spin-polarization of Fe, cause the deep pseudogap at the Fermi level between 60 and 63 VE and allow for stabilization of the structure.

Crystal Overlap Hamiltonian Population (−COHP) curves were also analyzed from these electronic structure calculations and the resulting curves are illustrated as the averaged spin-polarized interactions in Fig. 3 with the integrated values listed in Table 3. In addition, the Integrated COHP (−ICOHP) values for various interatomic contacts in this complex structure are compared with –ICOHP values evaluated for binary or elements species containing similar metal atom ratios and coordination environments. "$Zr_2FeRu_5B_2$" shows nonbonding Ru–B interactions at E_F and an averaged −ICOHP value of 2.93 eV/bond. The Ru–Zr interactions show bonding at E_F with the optimized interaction occurring at 67 VE (+0.9 eV). The Ru–Fe interaction shows nearly optimal bonding (–ICOHP=1.28 eV/bond) with the crossover at 65 VE. Ru–Ru interactions fall in an antibonding region, with the crossover well below E_F at 47 VE (−1.5 eV); however, the net interaction remains bonding. These results indicate a mostly filled Ru 4*d* band, which is seen in the partial DOS curve (Fig. 2).

The Fe–Fe orbital interactions were investigated along the [0 0 1] direction for the non-spin polarized case, illustrated in Fig. 4a, as well as for the decoupled majority and minority spins in Fig. 4b. The non-spin polarized Fe–Fe interaction is optimized at 60 VE (−0.32 eV) with E_F falling in a region of strongly antibonding states. Spin polarization optimizes the Fe–Fe interaction of the majority spin wavefunctions and shifts the crossover of the minority spin states to 63 VE (+0.20 eV).

The occupation of relatively narrow states at the Fermi level in a non-spin polarized calculations, states which are antibonding between magnetically active metal atoms, has previously been described to indicate ferromagnetic ordering [22–24]. Upon spin polarization, the energies of the majority spin states drop due to reduced screening, and the orbital overlaps decrease as the

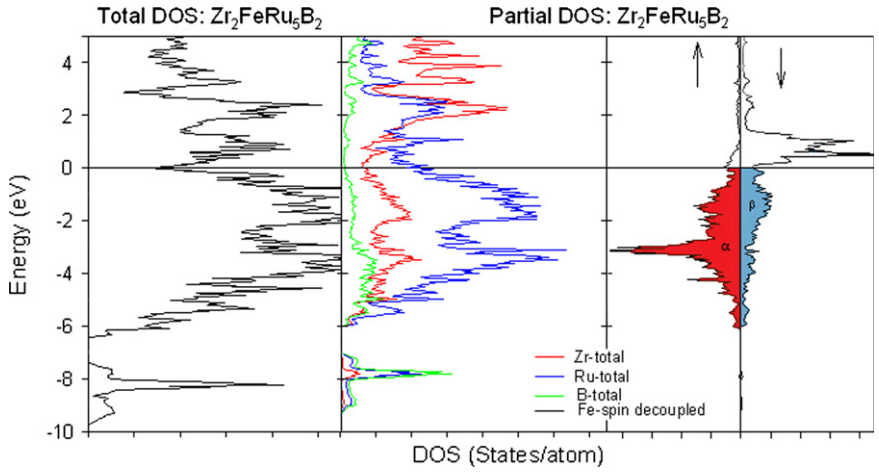

Fig. 2. Partial DOS curves of "$Zr_2FeRu_5B_2$" obtained from spin-polarized (LSDA) calculation plotted as the sum of "spin 1" and "spin 2" for the Zr, Ru, B. The individual spins for the magnetic Fe are also plotted with the ICOHP values shade with the α (red)=5.4 electrons and β (blue)=2.6 electrons (E_F is set to zero). (For interpretation of the references to color in this figure legend, the reader is referred to the web version of this article.)

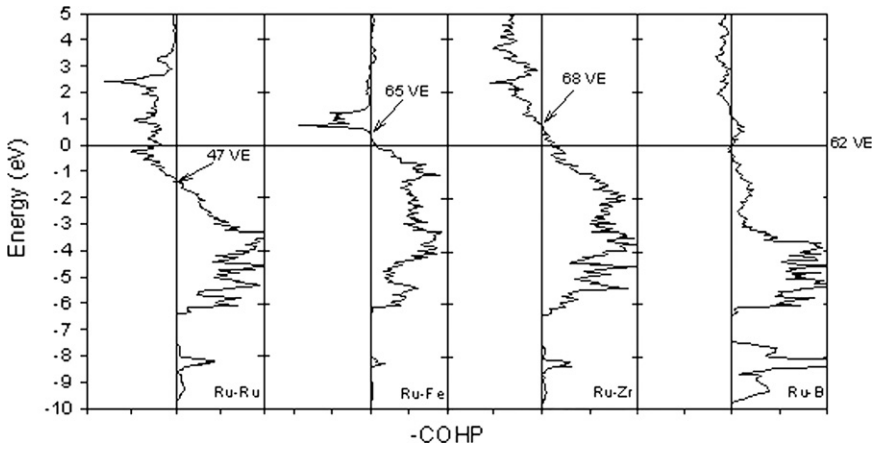

Fig. 3. Spin-polarized (LSDA) COHP curves for nearest neighbor contacts in "$Zr_2FeRu_5B_2$". (+ is bonding/− is antibonding, E_F is set to zero).

Table 3
Homoatomic and heteroatomic bonding for $Zr_2FeRu_5B_2$, associated −ICOHP values and literature structures with calculated −ICOHP values.

Bond	Distances (Å)	−ICOHP (eV/bond)	Bond	Distances (Å)	−ICOHP (eV/bond)
Ru–Ru	2.6–3.0	0.851–1.09	Ru–Ru (hcp)	2.67	1.69
				2.75	1.45
Ru–Zr	2.851	2.02	Ru–Zr ($ZrRu_2$) [19]	3.01–3.05	1.16–1.22
	2.947	1.58			
Ru–Fe	2.621	1.28			
Ru–B	2.225	2.93	Ru–B (Ru_8B_{11}) [20]	2.165	2.78
Fe–Fe [0 0 1]	3.067	0.44	Fe–Fe ($RbFeS_2$) [21]	2.702	0.58

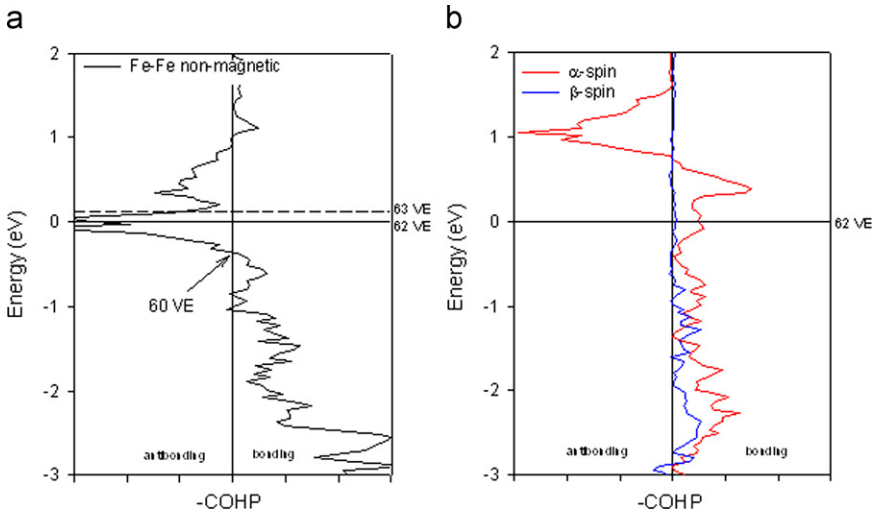

Fig. 4. (a) Nonmagnetic (LDA) COHP curves for the Fe–Fe contacts in the [0 0 1]. (b) Decoupled α (red) and β (black) spins. 62 VE: $Zr_2FeRu_5B_2$, 63 VE: $Zr_2FeRu_4RhB_2$. (E_F is set to zero). (For interpretation of the references to color in this figure legend, the reader is referred to the web version of this article.)

wavefunctions become less diffuse, so that both bonding and antibonding orbital interactions are reduced. On the other hand, the energies of the minority spin states increase and exhibit greater dispersion. The resulting Fermi level frequently sits at the crossover between bonding and antibonding states in the minority spin DOS [22–24]. Following this premise, the Fe–Fe interactions are predicted to be ferromagnetic. The increase in valence electron count by substituting Rh for Ru (from 62 to 63 VE) ("$Zr_2Fe(Ru/Rh)_5B_2$") is plotted as the dashed line in Fig. 4 using the rigid band approximation. The resulting Fermi level remains among antibonding states; so ferromagnetic behavior should remain. Magnetic coupling through bonds cannot be studied by the COHP analysis, so we did not evaluate these curves for distances between adjacent [0 0 1] chains.

Since the COHP curves can only be used to suggest magnetic ordering for near neighbor contacts and not through-bond couplings, various magnetically ordered models of "$Zr_2FeRu_5B_2$" were constructed to explore inter-chain magnetic orderings as

Table 4
Magnetic models to predict preferred magnetic ordering and local magnetic moments for a hypothetical composition, "$Zr_2FeRu_5B_2$".

Magnetic Model	AFM1	AFM2	AFM3	FM
Total energy (MeV/unit cell)	–	+63.1	+71.9	+120
Total moment (μ_B)	0	0	0	11.566
Local magnetic moment (μ_B/atom)				
Fe1 (1*a*)	2.981	±2.888	±2.931	2.931
Fe2 (1*b*)	−2.981	±2.888	±2.931	2.931
Ru1	0.068	0.000	0.000	0.022
Ru2	−0.068	0.000	0.000	0.022
Zr	0.000	−0.005	0.001	−0.037

well as alternative intra-chain antiferromagnetic (AFM) couplings. Four different models were constructed in the space group *P*4/*m* and required a unit cell doubled along the *c*-axis. The symmetry reduction from *P*4/*mbm* to *P*4/*m* splits the crystallographically equivalent 2*a* sites into two individual sites: 1*a* (0 0 0) and 1*b* ($\frac{1}{2}\frac{1}{2}$0), which is necessary for the magnetic models. See supporting information for illustrations of the four starting magnetic orderings. Local moments were placed exclusively on the Fe atoms as starting points for invoking spin polarization. All calculations were allowed to converge according to the same criteria, while the preferred model was selected by a comparison of the total energies per formula unit. These results are summarized in Table 4.

The most energetically favorable model (AFM1) contains ferromagnetic (FM) ordering along each Fe atom chain, and AFM ordering between these chains along {1 1 0} directions. The local magnetic moments at the Fe atoms in these chains are close to 3 unpaired electrons per Fe atom (2.981 μ_B). Nearest neighbor Zr atoms hold no magnetic moment, while the Ru atoms also contain small moments ordered ferromagnetically with respect to the closest Fe atom chain. The next most energetically favorable model (AFM2) contains AFM ordering within each chain, i.e., along [0 0 1], as well as between the chains along the {1 1 0} directions. The magnitudes of the local moments on the Fe atoms are slightly smaller than the AFM1 case; however, the nearest neighbor Ru atoms now develop zero magnetic moment. Changing the inter-chain ordering of these AFM chains to FM along the {1 1 0} directions, which is modeled in AFM3, further increases the total energy. The 8.8 meV/unit cell increase from AFM2 to AFM3 signifies the weak exchange coupling between the magnetic chains. The least energetically favorable model, FM, which involves FM coupling within and between chains, creates local moments of 0.022 μ_B/atom at the Ru atoms and small moments (0.037 μ_B/atom) also building upon the Zr (the moments at Zr counter the overall moments of the Fe and Ru sites). The magnitudes of the local moments on the Fe atoms are calculated to be similar for each magnetic model.

The results of analysis of the Fe–Fe intra-chain COHP curves as well as evaluation of total energies for different magnetic models complement each other. Both results agree that intra-chain Fe–Fe exchange coupling is preferentially FM for "$Zr_2FeRu_5B_2$" (62 VE). Total energies revealed that AFM coupling between near neighbor chains along the {1 1 0} directions is favorable over FM coupling, a result which could lead to an overall low net magnetization of these samples. A rigid band model was applied to predict the effect of Rh substitution on the total energies of each model: these energies of the different magnetic structures order identically to "ZrFeRu$_5$B$_2$." The local magnetic moments at the Fe sites are not affected by the Rh substitution, maintaining moments that are ca. ±2.9 μ_B/atom. The long range magnetic ordering for the isostructural and isoelectronic $Sc_2FeRu_3Rh_2B_2$ and $Sc_2FeRu_2Rh_3B_2$ both show ferromagnetism by experiment and theory [5,6]. The origin for these differences in magnetic order with composition and valence electron count for this entire class of magnetically responsive borides is currently under study.

Table 5
SQUID magnetic measurements of the bulk sample I and sample II.

	Sample I	Sample II
T_c (K)	239(2)	233(6)
θ (K)	129.0(9)	138(2)
μ_a (μ_B/Fe)	0.235(4)	0.373(4)
Coercivity (Oe)	1087(67)	323(1 2 2)
Remanence (μ_B/mol)	0.0250(3)	0.0710(6)

*μ_a at 5 K and 5 T.

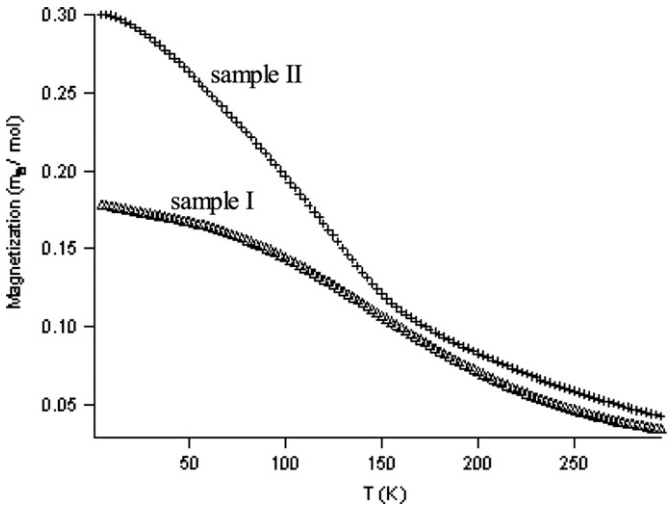

Fig. 5. Shown here are $M(T)$ curves at fields of 2.5 T. Both structures suggest ferrimagnetic ordering at ca. 230 K with a higher order transitions occurring in the Rh substituted sample ca. 150 K.

3.4. Magnetization measurements

The Curie temperatures (T_C), Weiss temperatures (θ), and μ_a values are listed in Table 5 for samples I and II. Both samples appear to be ferrimagnetic showing a hysteresis curve with small magnetic moments developing per Fe atom. However, neither specimen reaches saturation at 5 K and 5 T. Analysis of these magnetization results yield effective moments of 0.235(4) μ_B/Fe and 0.373(4) μ_B/Fe, respectively, for samples I and II at 5 K and B_0=5 T. Both loops show hysteresis with very small remanence and coercivity, features that are indicative of soft ferrimagnets.

The Curie temperatures were approximated by the intersection of a linear fit about the maximum dM/dT of the magnetization vs. temperature (M vs. T), see Fig. 5 [25]. A plot of χ^{-1} vs. T for sample

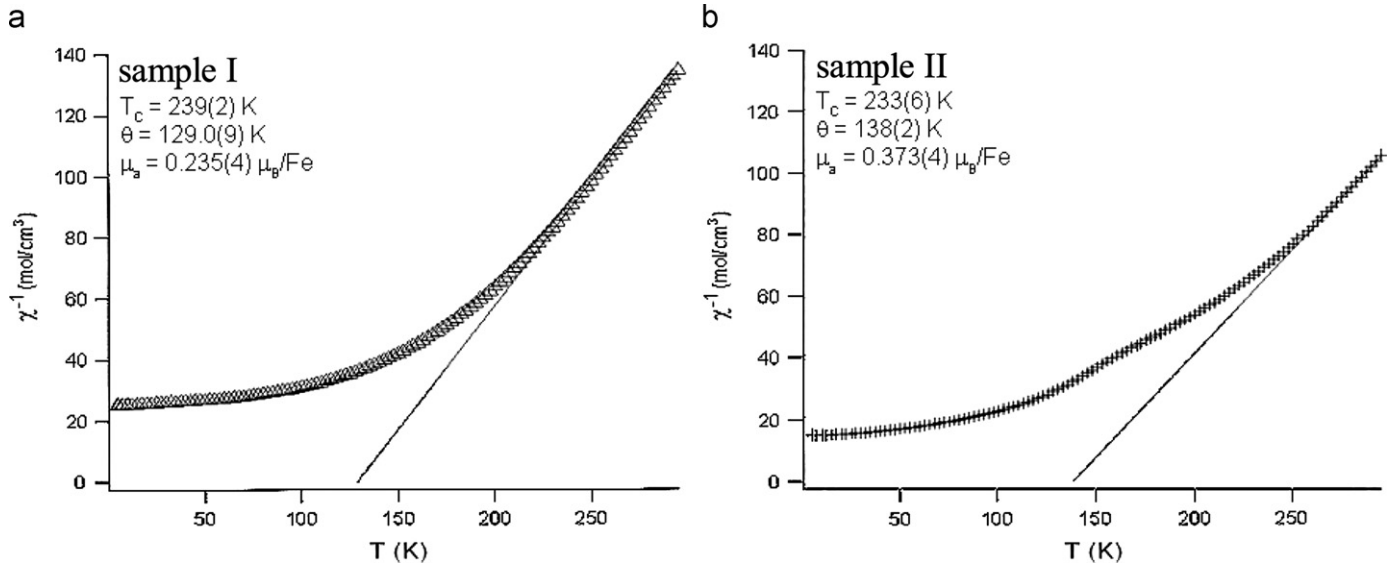

Fig. 6. (a) χ−1 versus T for sample I shows onset of Curie–Weiss behavior above 200 K. (b) χ^{-1} versus T for sample II with a fit of the paramagnetic region at the onset of Curie–Weiss behavior just under 300 K.

I in Fig. 6a follows Curie–Weiss behavior at temperatures exceeding ca. 220 K. Although the SQUID measurements were collected on the bulk multiphase sample, the data collected for sample I should originate solely from the desired phase. The secondary phase in sample I, $FeRu_2$, has been shown in previous work on hexagonal close packed Fe–Ru alloys to be a Pauli-paramagnet. In fact, with greater substitution of Ru, the magnetic moments drop dramatically above ca. 5 at% [26]. Furthermore, a theoretical investigation on the substitution of iron with a 4*d* metal also shows a dramatic decrease in the magnetic moment with greater substitution of 4*d* metal [27]. As a result of these factors, the magnetic moments in sample I most likely arise from the desired phase rather than any impurity phases.

A Curie–Weiss fit was performed for sample II in Fig. 6b, although the linear regime of the paramagnetic curve is near the upper limit of the temperatures probed. Due to the multiple phases present in sample II, interpretation of the data is much more complex. However, the Curie temperature and the Weiss temperature are close to sample I. Therefore, we believe the primary magnetic transition at ca. 230 K is a result of our desired phase and not the impurities. However, sample II shows a second magnetic transition present at 150 K, a transition that could be a result of an impurity, and is currently under investigation.

The magnetic moment per atom in sample I has a value that is approximately 10% of the theoretically predicted value (2.878 μ_B/Fe) and the electronically similar scandium analogue, $Sc_2FeRu_3Rh_2B_2$ (63 VE), which has a reported moment of 3 μ_B/Fe [5]. However, in both of these cases, the 2*a* site is fully occupied by Fe atoms. Previous theoretical work determined that Ru has a very small pairwise exchange, J_{Fe-Ru}=0.07 MeV, and thus limits magnetic coupling [6]. As a result, mixing of Ru and Fe at the 2*a* site, as seen in sample I, will likely disrupt any long range magnetic ordering. Additionally, Rh was shown to have a larger exchange (J_{Fe-Rh}=3.77 MeV) and, thus, enhance both magnetic exchange and the total magnetic moment of the system [5]. This is seen experimentally in the series $Sc_2Fe(Ru_{5-x}Ru_x)B_2$ (x=3, 4, 5) with the magnetic moments increasing from 3 to 3.1 μ_B/Fe to 3.3 μ_B/Fe depending on the level of Rh substitution. A similar result is found here with an increase in the magnetic moment by ca. 40% with Rh substitution. A further study on the effects of magnetic ordering with respect to atomic mixing at the 2*a* site is currently underway.

4. Conclusions

The isotypic structures, $Zr_2Fe_{0.87(8)}Ru_{5.13}B_2$ and $Zr_2Fe_{0.82(3)}(Ru/Rh)_{5.18}B_2$, have been prepared by high-temperature methods and structurally characterized to show partial mixing of Fe and Ru/Rh atoms independent of the total valence electron count. TB-LMTO electronic structure calculations of the nearest stoichiometric model, "$Zr_2FeRu_5B_2$", show strong polarization of the Fe atoms (2.98 μ_B/Fe) and weak polarization of the surrounding net of 4*d* metals Ru net (−0.04 to 0.002 μ_B/Fe), while the electronic structure of "$Zr_2FeRu_4RhB_2$" has been suggested by a rigid band approximation to the electronic structure of "$Zr_2FeRu_5B_2$". Ferromagnetic ordering was predicted via through a COHP analysis of the DOS, while mixed magnetic ordering is predicted from the total energies of the model systems. Finally, SQUID magnetic measurements show soft ferrimagnetism for both structures with smaller total moments than predicted theoretically. Neutron scattering, with an emphasis on magnetic scattering results, coupled with further theoretical studies of Fe-deficient models $Zr_2Fe_{1-\delta}(Ru_{1-x}Rh_x)_{5+\delta}B_2$ are warranted to substantiate these conclusions.

Acknowledgments

J.R.B. would like to thank Dr. Boniface Fokwa, Christian Goerens, Dr. Shalabh Gupta for many helpful discussions and Debanjan K. Ghosh for experimental assistance. EDS was collected with the assistance of the Materials Analysis and Research Lab (MARL) at Iowa State University. The authors acknowledge the generous financial support provided by the US National Science Foundation (NSF DMR 08-06507).

Appendix A. Supporting information

Supplementary data associated with this article can be found in the online version at doi:10.1016/j.jssc.2010.09.025.

References

[1] Y.B. Kuz'ma, Y.P. Yarmolyuk, Zh. Strukt. Khim. 12 (1971) 458.
[2] W. Jung, J. Schiffer, Z. Anorg. Allg. Chem. 581 (1990) 135.
[3] E.A. Nagelschmitz, W. Jung, Chem. Mater. 10 (1998) 3189.
[4] E.A. Nagelschmitz, W. Jung, R. Feiten, P. Müller, H. Lueken, Z. Anorg. Allg. Chem. 627 (2001) 523.
[5] B.P.T. Fokwa, L. Heiko, D. Richard, Chem.—A Eur. J. 13 (2007) 6040.
[6] G.D. Samolyuk, B.P.T. Fokwa, R. Dronskowski, G.J. Miller, Phys. Rev. B 76 (2007) 094404.
[7] B.A. Hunter, Rietica: A Visual Rietveld Program, 1.71; International Union of Crystallography, Commission of Powder Diffraction: 1997.
[8] J. Brgoch, G.J. Miller, Unpublished Results.
[9] STOE, X-SHAPE–crystal optimization for numerical absorption correction, 1.01; 1996.
[10] STOE, X-RED, data reduction program, 1996.
[11] G.M. Sheldrick, SHELXL-97, A Program for the Refinement of Crystal Structures, University of Göttingen, Göttingen, Germany, 1997.
[12] K. Brandenburg, DIAMOND: Visual Crystal Information System, CRYSTAL IMPACT, Bonn, Germany, 1999.
[13] O.K. Andersen, Phys. Rev. B 12 (1975) 3060.
[14] O.K. Andersen, O. Jepsen, Phys. Rev. Lett. 53 (1984)) 2571.
[15] G. Krier, O. Jepsen, A. Burkhardt, O.K. Andersen, TB-LMTO-ASA Program, 4.7; Max Planck Institute for Solid State Research, Stuttgart, Germany, 1995.
[16] U. von Barth, L. Hedin, J. Phys. C 5 (1972) 1629.
[17] R. Dronskowski, P.E. Blöchl, J. Phys. Chem. 97 (1993) 8617.
[18] A.H. Dwight, Trans. Metall. Soc. AIME 215 (1959) 283.
[19] H.J. Wallbaum, Naturwissenschaften 30 (1942) 149.
[20] J. Aselius, Acta Chem. Scand. 14 (1960).
[21] W. Bronger, A. Kyas, P. Muller, J. Solid State Chem. 70 (1987) 262.
[22] R. Dronskowski, K. Karol, L. Heiko, J. Walter, Angew. Chem. Int. Ed. 41 (2002) 2528.
[23] G.A. Landrum, R. Dronskowski, Angew. Chem. Int. Ed. 38 (1999) 1389.
[24] G.A. Landrum, R. Dronskowski, Angew. Chem. Int. Ed. 39 (2000) 1560.
[25] B.P.T. Fokwa, G.D. Samolyuk, G.J. Miller, R. Dronskowski, Inorg. Chem. 47 (2008) 2113.
[26] H. Fujimori, H. Saito, J. Phys. Soc. Jpn. 26 (1969) 1115.
[27] B. Drittler, N. Stefanou, S. Blügel, R. Zeller, P.H. Dederichs, Phys. Rev. B 40 (1989) 8203.